PNAS
www.pnas.org

Supplementary Information for

Rapid growth of organic aerosol nanoparticles over a wide tropospheric temperature range

Dominik Stolzenburg et al.

Paul Winkler
E-mail: paul.winkler@univie.ac.at

This PDF file includes:

www.pnas.org/cgi/doi/10.1073/pnas.1807604115

Supporting Information Text

Measurement of particle growth with the appearance time method

Particle-size-distributions are measured by several sizing instruments optimized for a certain size range. Each instrument was thereby treated separately but we found comparable results in the overlapping regions for all presented experiments. Particle growth rate measurements were performed with the appearance time method, which can be used especially in chamber experiments, where a clear front of a growing particle population can be identified during most nucleation experiments.

Key part of this study is the precision measurement of particle-size-distributions in the size range between 1.8-8 nm by a newly developed instrument, a DMA-train (1). It uses six differential mobility analyzers in parallel with the classified size fixed for every device. Subsequent detection of the size-selected aerosol is done by the usage of six condensation particle counters. As no scanning is involved, high counting statistics at a single size is achieved, providing unprecedented high sensitivity to low number concentrations in the crucial sub 10-nm range. At diameters above 5 nm higher counting statistics allow one DMA to be set alternating every 10 seconds between 6.2 and 8 nm, hence providing in total seven measured sizes for the DMA-train: 1.8, 2.2, 2.5, 3.2, 4.3, 6.2, 8.0 nm (see Fig. S1 (B)).

The other size-ranges were covered by three additional instruments: Below 2.5 nm, a particle size magnifier in scanning mode was used (2). Above 8 nm a scanning mobility particle sizer system, TSI nano-SMPS model 3982, measured up to 65 nm (3). Additionally, a neutral cluster and air ion spectrometer (NAIS) measured between 3-42 nm (4). For the size distribution of particles >10 nm two additional SMPS systems were attached to the chamber, but were not used for detailed growth rate analysis.

Considering the evolution of particle size-distribution binned into different size-channels as given by most particle size-distribution measuring instruments, the signal in each size-channel is fitted individually with a four parameter sigmoid function using a least-square algorithm:

$$S_{\mathrm{d_p}}(t) = \frac{a-b}{1+(t/t_{\mathrm{app}})^d} + b, \qquad [1]$$

where a and b represent the background and plateau value of the sigmoid function respectively, d is a parameter for the steepness of the rising signal and t_{app} is the time at which the 50 % value between plateau and background is reached.

A representative fit for a 3.2 nm size channel of the DMA-train is shown in Fig. S1 (A). All size-channels are cross-checked manually after the automated fitting and a statistical error of t_{app} is estimated from the covariance of the fit-result. The values obtained for t_{app} can be plotted against the corresponding diameter as shown in Fig. S1 (B). A linear fit with an orthogonal distance regression is used to take into account both the uncertainties of t_{app} and of the diameter of the size-channels. The resulting value of the slope and its associated error can be interpreted as an apparent particle growth rate and its statistical uncertainty.

For the DMA-train two size-intervals for the growth rate measurement were defined: One between 1.8-3.2 nm and one between 3.2-8 nm. The choice of the size-intervals is arbitrary but proofed to be representative to show differences between early and later growth. In (5) it was shown that growth driven by biogenic organics shows only a minor size-dependence above 5 nm, i.e. the upper growth rate size-interval of the DMA-train is representative for growth >5 nm.

However, this apparent growth rate of the particle size distribution does not necessarily represent the growth caused by pure condensation, as it omits coagulation and, in chamber experiments, wall losses, which both alter the particle size-distribution (6). Therefore, a systematic uncertainty of the method is estimated to be 50 % (7). On the other hand, methods accounting for coagulation and loss effects do need reliable absolute number concentration measurements and therefore good knowledge of overall detection efficiencies of the sizing instruments. In the presented experiments there might be high uncertainties due to possible evaporation effects of particles produced at e.g. cold temperatures and brought into warmer analyzing instruments. To ensure precise sizing at different chamber temperatures, the sheath-air of all six DMAs of the DMA-train was passed through an heat exchanger maintained at chamber temperature. All inlet lines and sheath flow lines as well as the DMAs were insulated to be maintained as close to chamber temperature as possible. Subsequent evaporation losses inside the detecting CPCs are unlikely to affect the appearance time method. This method does not depend on absolute particle concentrations as long as there is enough signal detected in a channel to get reliable results with the fit by Eq. 1. To further investigate possible effects of particle evaporation on the measured growth rates a custom-build SMPS was operated while being completely contained inside a refrigerator which was kept at chamber temperature for the experiments at +5°C and -25°C. A comparison of this cooled SMPS with the nano-SMPS used in this study is presented in Fig. S2. The differences in absolute concentrations are within a factor of 2 and the growth rate measurements inferred are generally agreeing within the measurement uncertainties. We therefore conclude that the results of the appearance time method should be generally robust with respect to possible evaporation of the sampled particles and the major uncertainties are covered within the 50 % systematic error given by (7).

Absolute HOM concentration measurements using nitrate-CI-APi-ToF

The nitrate-CI-APi-ToF (nitrate-CI) uses negative nitrate, $(HNO_3)_n(NO_3^-)$, as reagent ion (8), which shows high charging efficiencies towards H_2SO_4 and HOMs. This rather selective ionization technique is used obtain a very clean spectrum of HOMs (9). The concentration of a HOM species is estimated via

$$[\mathrm{HOM}_i] = C \cdot T_i \cdot \mathrm{SL}_{\mathrm{HOM}_i} \cdot \ln\left(1 + \frac{[\mathrm{HOM}_i \cdot \mathrm{NO}_3^-]}{\sum_{j=0}^{2}[\mathrm{NO}_3^- \cdot (\mathrm{HNO}_3)_j]}\right) \qquad [2]$$

Here $[\mathrm{HOM}_i \cdot \mathrm{NO}_3^-]$ is the background corrected peak area which is normalized to the intensity of the main reagent ions. To obtain a quantitative concentration, three factors are applied: First, a calibration factor C, which is inferred from a calibration using sulfuric acid (10) and assuming that all detected HOMs have the same ionization efficiency (9). Second, a mass dependent transmission efficiency T_i of the APi-ToF can be inferred in a seperate experiment by depleting the reagent ions with several perfluorinated acids (11). Third, sampling line losses $\mathrm{SL}_{\mathrm{HOM}_i}$ are estimated assuming laminar flow diffusional losses in the sampling lines (12) with a diffusion coefficient of HOMs scaling with the molecular mass M_i of the compound via $D[\mathrm{cm^2 s^{-1}}] = 0.31 \cdot M_i^{-1/3}$ at 278 K, determined from wall loss measurements in the CLOUD chamber. As the sampling lines of the nitrate-CI are thermally insulated, for other experiment temperatures $D \propto (T/278K)^{1.75}$ is assumed. As the compounds detected by the nitrate-CI are mostly classified ELVOC or LVOC in the temperature range of this study, we can assume that they all get lost irreversibly to sampling line walls due to diffusion.

Absolute concentration measurements of oxidized organics using PTR3-ToF

The PTR3-ToF (PTR3) uses $(H_3O^+)(H_2O)_n$ clusters as reagent ions, ionizing α-pinene as well as first and higher order oxidation products by proton transfer or ligand switch reactions (13). A contact minimized laminar flow inlet system with core sampling is used to transfer the sample air into the tripole reaction chamber operated at 80 mbar and reduces transmission losses. The $(H_3O^+)(H_2O)_n$ cluster ion distribution can be regulated by a radio-frequency-amplitude applied to the tripole rods without influencing the reaction time. Increased pressure in the reaction region and longer reaction times compared to traditional PTR instruments yield a 500 fold increased sensitivity to a broad range of organics. At the operating conditions of the PTR3, secondary reactions of ionized species with the most abundant neutral VOCs in the sample gas are limited to less then one percent at the highest measurable concentrations. The new instrument bridges the gap between precursor measurements at ppbv level to HOM measurements at sub ppt level, complementing atmospheric pressure CIMS techniques.

A quadrupole interfaced Long-ToF mass spectrometer (TOFWERK AG, Thun, Switzerland) is providing the high mass resolving power needed to separate isobaric compounds. We obtained more than 1500 individual mass peaks, excluding isotopes, during α-pinene ozonolysis experiments. A multi-peak fitting algorithm is applied to separate the major compounds and assign chemical sum formulas. Extracting the relevant signals is done omitting all masses rising less than 3σ above chemical background noise during ozonolysis measurements and removing peaks with possible uncertainties caused by interference of higher neighboring peaks. $(H_3O^+)(H_2O)_n$ clusters are known to be soft ionization reagent ions. Nevertheless we cannot exclude completely fragmentation of some ionized HOMs loosing most likely H_2O especially when containing an (-OOH) group.

The PTR3 was calibrated with a gas standard containing 1 ppm of 3-hexanone, heptanone and α-pinene in nitrogen, which was dynamically diluted by a factor of 1000 in VOC-free air to contain 1 ppbv of each compound. Duty cycle corrected counts per second *dcps* are used in order to compensate for the mass-dependent transmission of the TOF mass spectrometer ($dcps(i) = cps(i) \cdot (101/m_i)^{1/2}$) (13). For 3-hexanone and heptanone we obtained a sensitivity which is in agreement with the calculated sensitivity taking into account the duty cycle corrected $(H_3O^+)(H_2O)_n$ regent ion count rates, the pressure and the reaction time in the reaction chamber (80 mbar; 3 ms) and using $2 - 3 \cdot 10^{-9} \mathrm{cm^3 s^{-1}}$ as a fast reaction rate constant close to the collisional limit value. Consequently, only lower end product concentrations can be given.

In a previous α-pinene ozonolysis study PTR3 results showed quantitative agreement for several HOMs with the nitrate-CI (13). The authors estimated 80 % inlet losses for low volatility molecules with $n_O \geq 5$, bringing the two instruments into reasonable quantitative agreement for common molecular ion signals. However, the assumption for the nitrate-CI, that all detected molecules get lost on contact with sampling line walls, does not hold for all substances measured by the PTR3. In the transition from SVOC to LVOC the partitioning of substances between inlet line walls and sample gas is temperature dependent. We therefore extended the approach of (13) with our knowledge about an approximate volatility of the measured compounds. Assuming that all molecules in the LVOC and ELVOC range get lost by diffusion (the diffusion coefficient of a molecule is estimated similar to the nitrate-CI) according to (12), we can apply a temperature dependent loss-correction for the sampling line losses, which is split up into three sections:

$$\eta_{\mathrm{tot}} = \eta_{\mathrm{line,int}}(T) \cdot \eta_{\mathrm{line,ext}}(298\mathrm{K}) \cdot \eta_{\mathrm{PTR3}}(310\mathrm{K}) \quad [3]$$

We account for losses at the sampling line within the CLOUD chamber $\eta_{\mathrm{line,int}}$ at chamber temperature T, as well as losses occurring at the sampling line outside the chamber at room temperature $\eta_{\mathrm{line,ext}}$ (as it was not thermally insulated) and losses within the PTR3 instrument heated to 37°C η_{PTR3}. Therefore, for each sampling section other molecules might be subject to losses according to their temperature-dependent volatility classification.

Comparison of the used mass spectrometers

The considerations of the two previous sections result in the comparison for data obtained in three representative experiments at three different temperatures which is shown in Fig. S3, where $\eta_{\mathrm{line,int}}$ and $\eta_{\mathrm{line,ext}}$ are calculated assuming diffusional losses similar to the nitrate-CI and η_{PTR3} is estimated to correct for the 80% discrepancy found in (13).

For higher oxygenated molecules the agreement between both mass spectrometers is in a reasonable range including the additional loss term η_{PTR3} for losses within the PTR3 ion source and inlet. This indicates that the loss in measured concentration from +25°C to -25°C for the three experiments at similar initial precursor oxidation rates is caused by the reduced reaction rates of the auto-oxidation process. For lower temperatures and lower oxidized states ($n_O = 4/5/6$) a discrepancy between the instruments gets significant. However, even at elevated temperatures, the nitrate-CI is only detecting a small fraction of all

oxidation products with $n_O = 5/6$ observed by the PTR3. Therefore it is concluded that the increasing discrepancy is likely due to a lowered sensitivity of the nitrate-CI for such compounds. The ionization efficiency in the nitrate-CI depends on the relative binding energy of a $(HNO_3)(NO_3^-)$ cluster compared to a $(Analyte)(NO_3^-)$ cluster (14). A relative shift in binding energies at lower temperatures that favors $(HNO_3)(NO_3^-)$ clustering instead of $(Analyte)(NO_3^-)$ clustering, could explain the observed decrease of signal for the lower oxidation states for the nitrate-CI. The higher oxidation states however are unaffected because the $(HOM)(NO_3^-)$ clustering is generally very strong and will always dominate the $(HNO_3)(NO_3^-)$ clustering, which explains the good agreement of the two instruments for higher oxidized states.

When combining the two mass spectrometers, for molecular ion signals observed in both instruments the higher signal is used. Both spectra are background subtracted and therefore a weaker signal in either of the mass spectrometers could point towards a lower ionisation efficiency.

Combined gas-phase mass defect plots

Fig. S4 shows mass defect plots from the nitrate-CI and the PTR3 during three representative experiments at three different temperatures. For all three cases the α-pinene ozonolysis rate is comparable.

The mass defect plots for all temperatures show the typical pattern of HOMs (5). Two bands can be identified, one representing monomers (n_C=6-10, 100-400 Th) and one representing dimers (n_C=16-20, 400-600 Th); molecules with increasing oxidation state are found towards the lower right of the panels. The reduction in temperature mainly reduces the signal of the higher oxygenated compounds towards the lower right of the panels. This is in agreement with (15) and the observation of reduced auto-oxidation rates at lower temperatures leading to less highly oxygenated molecules (16). This trend is as well shown in Fig. 5 for some representative molecules.

The symbol color for peaks with an identified composition in Fig. S4 corresponds to a broad temperature-dependent classification of their volatility, based on the carbon and oxygen numbers of the individual compounds. We place them in four general groups, according to their saturation mass concentration C^*: extremely low volatility compounds (ELVOC, $\log_{10} C^* \leq$-4.5), low volatility compounds (LVOC, $\log_{10} C^*$=(-4.5,-0.5]), semi-volatile compounds (SVOC, $\log_{10} C^*$=(-0.5,2.5]) and intermediate volatility compounds (IVOC, $\log_{10} C^* >$2.5) (17). Compounds in the ELVOC and LVOC ranges have been shown to contribute to nanoparticle growth (5). Comparing this classification for the three different temperatures clearly indicates the importance of the compounds observed by the PTR3. At -25°C, large quantities of LVOC compounds can be observed by the usage of this additional ionization technique.

FIGAERO-CIMS: Measurement procedure, data analysis, normalization on aerosol mass and thermogram fitting

Chemical composition of the bulk particle phase composition was measured by the Filter Inlet for Gases and Aerosols (FIGAERO) (18) coupled to a chemical ionization time-of-flight mass spectrometer (CI-ToF-MS) (Tofwerk, HTOF). Measurement cycles were set to 30 minutes particle sampling at 8 SLPM sampling flow rate, followed by a thermal desorption ramp (10 minutes, maximal heating rate). The particle phase sampling line outside of the thermal housing (∼0.5 m) of the CLOUD chamber was insulated, and due to the high sampling flow rates we assume that $T_{\mathrm{chamber}} \approx T_{\mathrm{sampling}}$. Desorption temperature in the FIGAERO is measured by a thermocouple installed in front of the particle filter. The particle filter was exchanged approximately every 48 hours between the experiments (Zefluor membrane, 2.0 μm pore size, 25 mm diameter, PALL, USA). The thermal desorption gas flow was 2 SLPM ultrapure synthetic air (from the CLOUD liquid nitrogen and oxygen reservoirs). O_2^- ions are formed by passing a 2.2 SLPM flow of synthetic air through a radioactive charger (^{210}Po, 370 MBq, Model P-2021, NRD Inc., USA) and into the ion molecule reaction (IMR) chamber, where the chemical ionization occurs. The body of the IMR was heated to approximately 50°C to avoid condensation of low volatility compounds and kept at 800 mbar using an active pressure control device (Aerodyne Inc., USA). The voltages of the transfer optics were tuned for maximum sensitivity and strong declustering in order to minimize cluster ions and maximize the signal of $[M\text{-}H]^-$ ions. Blank particle phase samples were obtained between the chamber experiments by continuous sampling or by manually switching a HEPA filter in front of the FIGAERO filter during the experiments. Gas phase concentrations of the majority of oxidation products were too low throughout all experiments to be monitored in real-time by the gas-phase sampling position of the FIGAERO.

Data analysis using Tofware (version 2.5.11_FIGAERO) gave 10 seconds average mass spectra. A post-acquisition mass calibration using the ions O_2^-, CO_3^-, NO_3^-, HCO_4^- and $C_{16}H_{31}O_2^-$ resulted in a mass accuracy <10 ppm. High-resolution peak identification of the particle phase products was done with the constraints of n_C: 1-20, n_H: 2-50, n_O: 0-20. Shoulder peaks were fitted also when no ion was identified, in order to resolve background signal from varying analyte signal. The ion signal [ions/s] was normalized by the reagent ion signal $((O_2^- + CO_3^-)\cdot 10^{-6})$, where 10^6 is the reference value. Selected high-resolution ion traces ($C_{10}H_{15}O_{3-9}^-$) of the FIGAERO desorption ramps of three experimental runs at T=-25, +5 and +25°C were further processed: The aerosol mass collected (M_{coll}) per FIGAERO filter cycle was calculated by the product of FIGAERO sampling flowrate and integrated mass of the combined nanoSMPS and SMPS particle size distribution. Aerosol density was approximated with $1.5\,\mathrm{g\,cm^{-3}}$. For sampling cycles during which $M_{\mathrm{coll}} > 10$ ng (Fig. S5), the FIGAERO ion signal was normalized by the sampled mass, providing the thermograms shown in Fig. 4 and enabling quantitative comparison between results at different temperatures. The number of thermal desorptions (n_{Des}) are 31, 12 and 15 for the experiments at -25°C, +5°C and +25°C, respectively. Mean and standard error of the mean are calculated from the results of a cubic smoothing spline fit (smoothparam=0.01) for each normalized thermogram, resulting in the thick lines and shaded areas in Fig. 4, respectively. During desorption, we observed a lower effective heating rate for the low temperature experiments, since

the tubing and the FIGAERO filter material cooled down during sampling. This observation explains different T_{max} for the same molecular formulas in the thermograms. Thermograms of monomeric ion signals often exhibit a mode that originates from fragment ions of compounds that decompose at high temperatures (19). For most monomeric ion signals we observed bimodal thermograms, indicating that thermal decomposition during the temperature ramping is a significant phenomenon. Therefore, we fitted the thermograms with three modes (monomer mode, dimer (decomposition) mode and background mode) at different temperature boundaries using a fitting function used in chromatography (20). A non-linear least squares solver (lsqcurvefit, Matlab) was applied for fitting the thermograms and extracting the peak areas from the monomer mode.

Growth rate parametrization

Growth rates were parametrized in Fig. 2 (A) and (B) by the simple exponential relation GR=$m(T, d_p) \cdot [\mathrm{k}(T) \cdot \mathrm{ap} \cdot \mathrm{O_3}]^q$, to express the correlation between growth rate and α-pinene ozonolysis reaction rate. While the coeffcients $m(T, d_p)$ depend on temperature and size-range of the growth rate measurement, q is chosen to be independent of both. A minimum least-square regression yields the results presented in Table S1.

Volatility of HOMs

Direct measurements of volatilities of individual HOM are extremely challenging as they are difficult to synthesize and the vapour pressures are too low for current volatility measurement techniques. To overcome this problem, vapour pressures can be inferred by several model calculations, like so-called group contribution methods (21) or parametrizations according to the oxidation state (17). In this study a combined approach is applied.

We use a volatility parametrization according to the carbon n_C^i and oxygen n_O^i number of the specific molecule i. This is based on two general observed trends that increasing carbon and increasing oxygen number lower the volatility of oxidized organic molecules. Thus, these quantities are linked to volatility, expressed as the logarithm of the saturation mass concentration $\log_{10} C_i^*$ for compound i:

$$\log_{10} C_i^*(300K) = \left(n_\mathrm{C}^0 - n_\mathrm{C}^i\right) \cdot b_\mathrm{C} - n_\mathrm{O}^i \cdot (b_\mathrm{O} - b_\mathrm{add}) - 2\frac{n_\mathrm{C}^i n_\mathrm{O}^i}{n_\mathrm{C}^i + n_\mathrm{O}^i} b_\mathrm{CO} \quad [4]$$

where the parameter n_C^0=25 is the baseline carbon backbone for a volatility of 1 μg m^{-3} without the addition of any functional groups. b_C=0.475 is the roughly half decade decrease in volatility per carbon atom and b_O=2.3 is the more than two decade decrease in volatility per oxygen atom assuming an average of (=O) and (-OH) groups. b_CO is a non-linearity term. More details can be found in (17).

However, other functionalities e.g. hydroperoxides (-OOH) and covalently bound dimers are not included in b_O, but are both abundant in HOMs from α-pinene ozonolysis. To account for these specific attributes, a representative set of proposed products (5, 22) with known structure is analyzed with the group contribution method SIMPOL (21). The results are fitted with Eq. 4 including a free parameter b_add altering the effect of oxygen b_O. Monomer and dimer products are fitted separately allowing this parameter to include the covalent binding.

The resulting parametrisation at 300 K is shown in Fig. S6. The free parameter yields $b_\mathrm{add} = 0.90$ for monomers and $b_\mathrm{add} = 1.13$ for dimers. Accordingly, for any α-pinene ozonolysis product with unambiguously identified composition, a volatility can be calculated.

However, computed volatilities from group-contribution methods generally tend to underestimate vapour pressures at low vapour pressures. A recent study investigating the volatility of α-pinene oxidation products with quantum-chemical based model calculations found large deviations due to intramolecular H-bonds (22). These deviations were significant especially for highly oxygenated monomers and dimers, while the agreement for the higher volatilities was much better.

This study focuses on the temperature dependence of the volatilities which is described by:

$$\log_{10} C^*(T) = \log_{10} C^*(300K) + \frac{\Delta H_\mathrm{vap}}{R \ln(10)} \left(\frac{1}{300} - \frac{1}{T}\right) \quad [5]$$

The evaporation enthalpy ΔH_vap can be linked to the saturation mass concentration at 300 K $\log_{10} C^*(300K)$ according to (17) and combined with (23):

$$\Delta H_\mathrm{vap} \left[\mathrm{kJ\,mol^{-1}}\right] = -5.7 \cdot \log_{10} C^*(300K) + 129 \quad [6]$$

The correlation between volatility at 300 K and the evaporation enthalpy ΔH_vap is very comparable for approaches like (23), (17) and (22). Moreover, the shift in volatility due to temperature in this study is most important for oxygenated compounds with volatilities around $\log_{10} C^*(300K) \approx 0$, at the transition between LVOC and SVOC. For those molecules also the predictions of the volatility between the different methods don't differ drastically (22). Therefore, we assume an overall uncertainty of the volatility description of ± 1 bin (i.e. 1 decade in $C^*(300K)$ for volatility distributions within a volatility basis set). This uncertainty is shown Fig. 2 (E) and (F) and gives the method uncertainties in Fig. 3.

Aerosol growth model

The measured VBS-distributions can be used to model aerosol growth. The modeling framework is based on the one used in (5) but simplified for the input of direct VBS-distribution measurements. Starting from a VBS-distribution at $t = 0$ the growth of a monodisperse population of nucleated particles at an initial size of 1.2 nm mobility diameter is modeled. Every VBS bin is treated like a single surrogate molecule having the properties of the averaged mass and concentration of the bin. It is assumed that the measured gas-phase concentrations are in steady-state with losses to particles and chamber walls. The condensation flux $\phi_{i,p}$ of every VBS bin i should then follow:

$$\phi_{i,p} = N_p \cdot \sigma_{i,p}, \cdot k_{i,p} \cdot F_{i,p} \quad [7]$$

N_p gives the number concentration of particles of a given size. $\sigma_{i,p} = \pi/4(d_p + d_i)^2$ is the particle-vapor collision cross-section including the diameter of the monodisperse particle population d_p and mass-diameter of the VBS bin d_i. $k_{i,p} = \alpha_{i,p}\nu_{i,p}\beta_{i,p}$ is the deposition rate of vapor molecules at surface, with $\alpha_{i,p}$ the mass accommodation coefficient, $\nu_{i,p} = (8RT/(\pi\mu_{i,p}))^{1/2}$ the center of mass velocity for particle and vapor (with the reduced mass $\mu_{i,p} = (M_i M_p)/(M_i + M_p)$) and $\beta_{i,p}$ the correction factor for non-continuum dynamics (24). $F_{i,p}$ is the driving force of condensation, closely related to the saturation ratio S_i of the VBS bin by $F_{i,p} = C_i^0(S_i - X_{i,p}\gamma_{i,p}K_{i,p})$. This driving force of condensation for a VBS bin i gives the difference between gas phase activity S_i and particle phase activity $(X_{i,p}\gamma_{i,p}K_{i,p})$, which includes the Raoult term $X_{i,p}\gamma_{i,p}$ to account for the mixture effect of the particles and the Kelvin-term $K_{i,p} = \exp(4\sigma M/(RT\rho d_p))$ accounting for the curvature effect of the particle surface. The model assumes an ideal mass based solution, i.e. the condensed phase activity is the mass fraction $X_{i,p}$ and hence $\gamma_{i,p} = 1$. Therefore we use $C*$ as saturation mass concentration throughout this study, as $C^* = \gamma_{i,p}C^0$.

Solving the above condensation equations for the measured evolution of the VBS-distribution assuming this distribution always reflects a steady-state between production from α-pinene ozonolysis and wall losses and following the growing monodisperse aerosol population, yields a diameter versus time evolution which can be connected to a growth rate.

Besides from the different input VBS-distributions at different temperature, only the Kelvin-term and the collision-frequency include a temperature dependence.

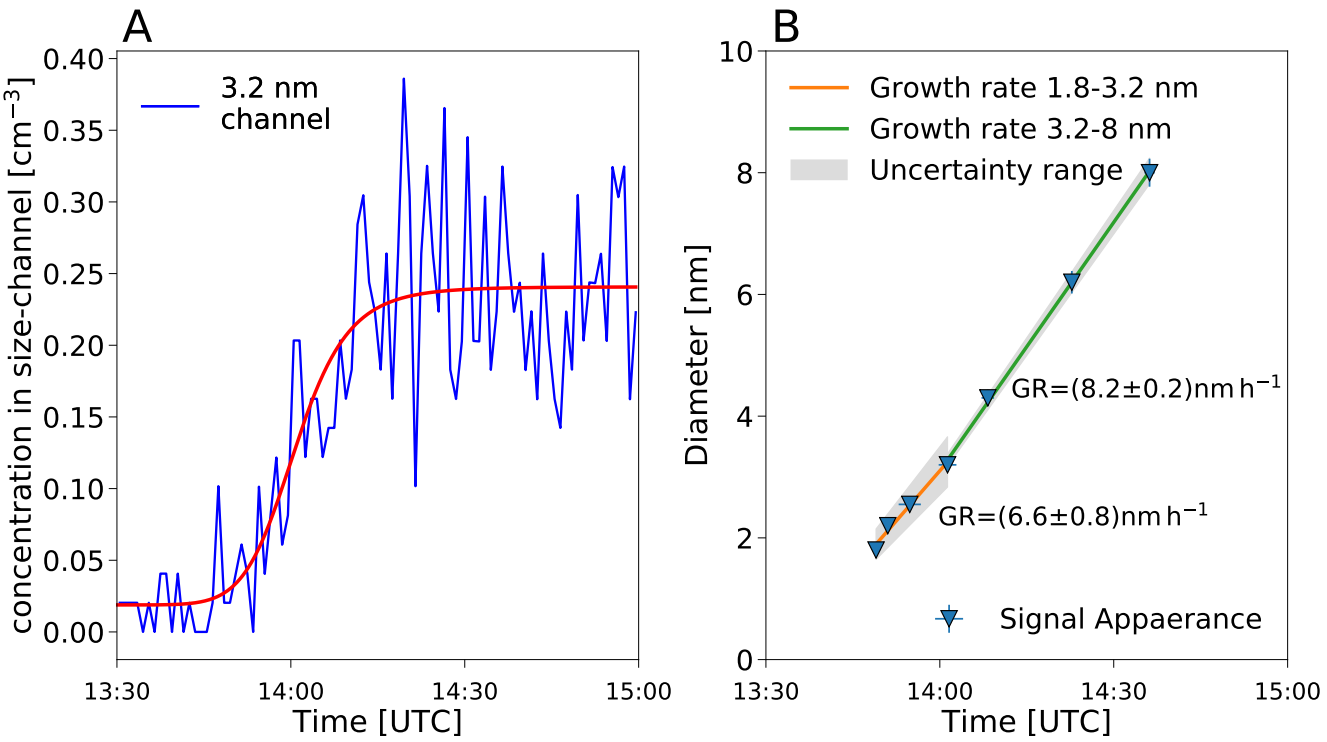

Fig. S1. Example for a representative determination of the particle growth rate with the appearance time method for data obtained by the DMA-train. (A) shows the sigmoid function fit to the measured concentration within the 3.2 nm channel. (B) shows the orthogonal distance regression for the growth rate determination in two intervals.

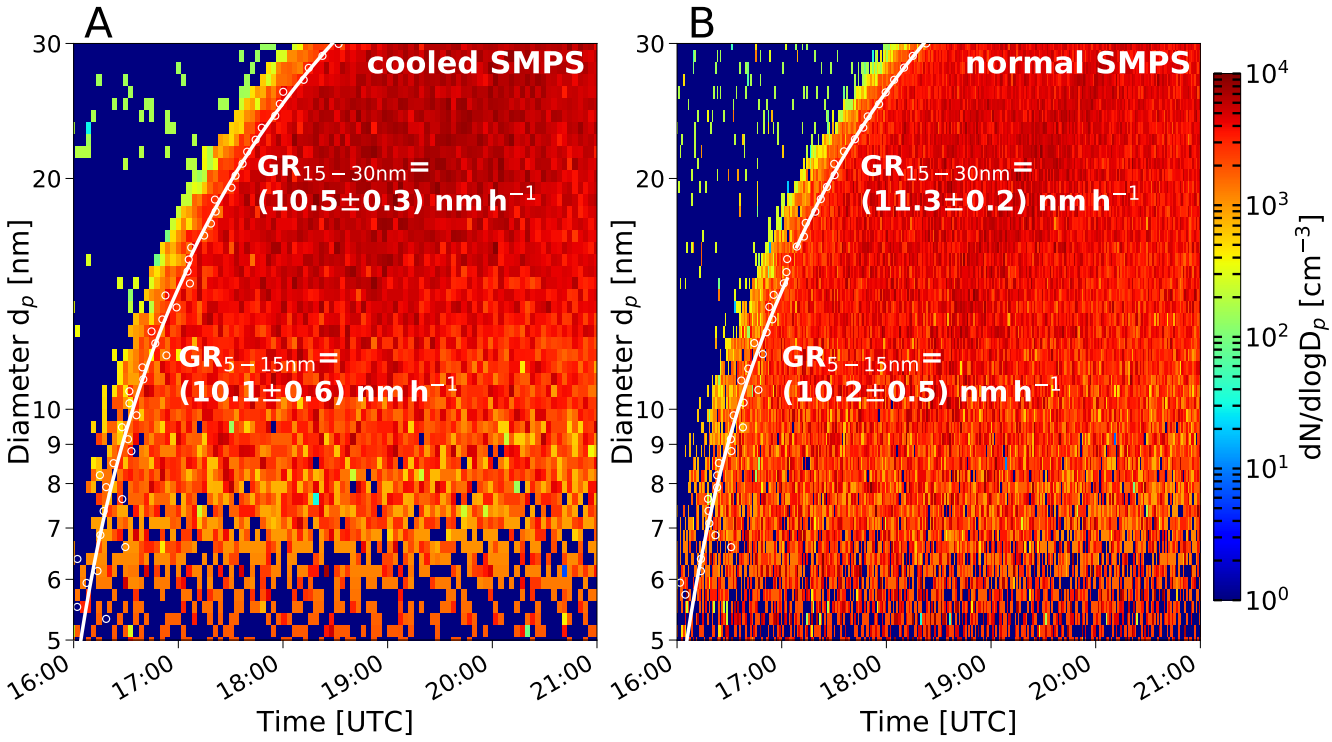

Fig. S2. Comparison of a completely cooled (kept at chamber temperature) and normal SMPS (operated at ambient temperature) during a dark α-pinene ozonolysis experiment at +5°C. White circles and lines show the appearance time growth rate estimation. Note that both instruments have slightly different time-resolution.

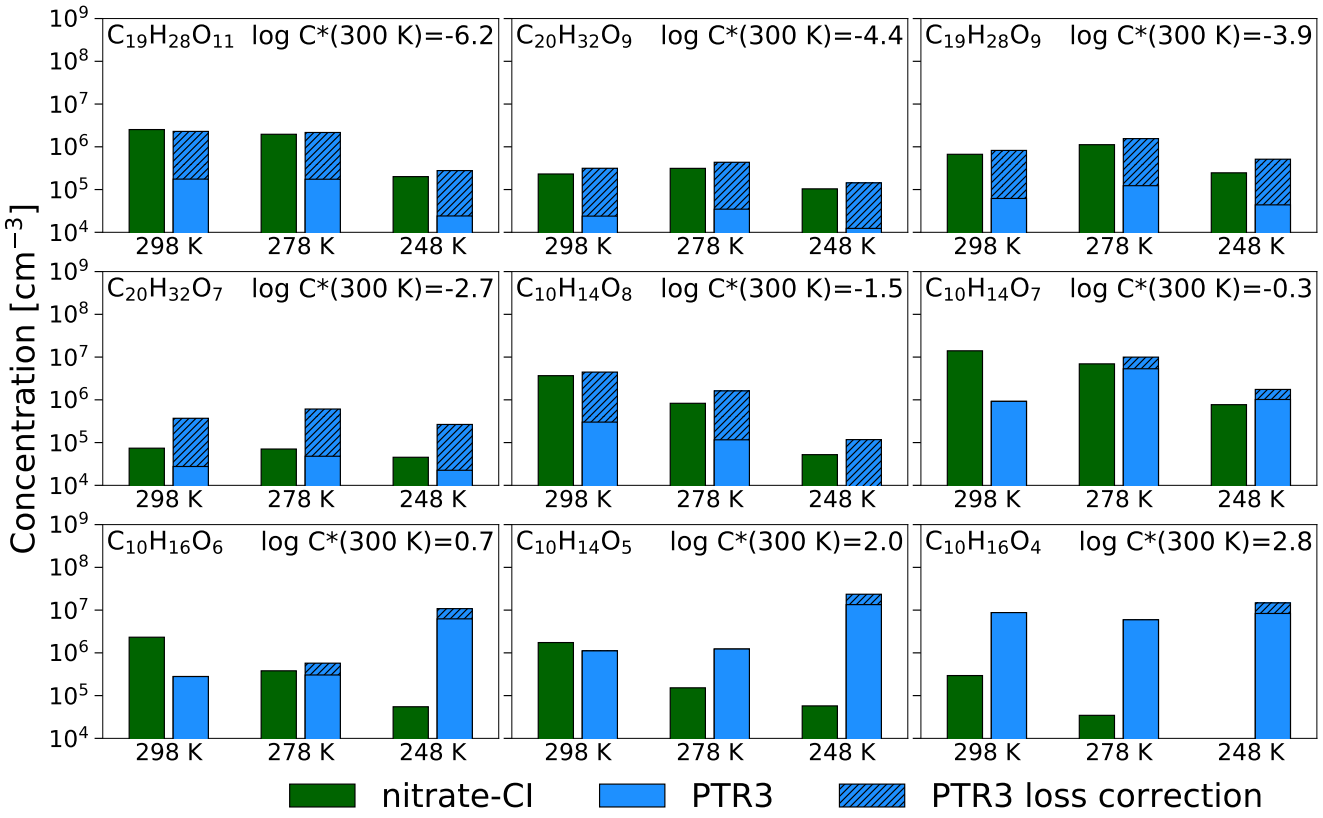

Fig. S3. Quantitative comparison of selected peaks observed in both mass spectrometers and its temperature dependence for three representative runs with similar α-pinene ozonolysis rate. The correction for PTR3 compounds to account for sampling line losses and the additional 80 % wall loss inside the PTR3 ion source are displayed by the hatched area.

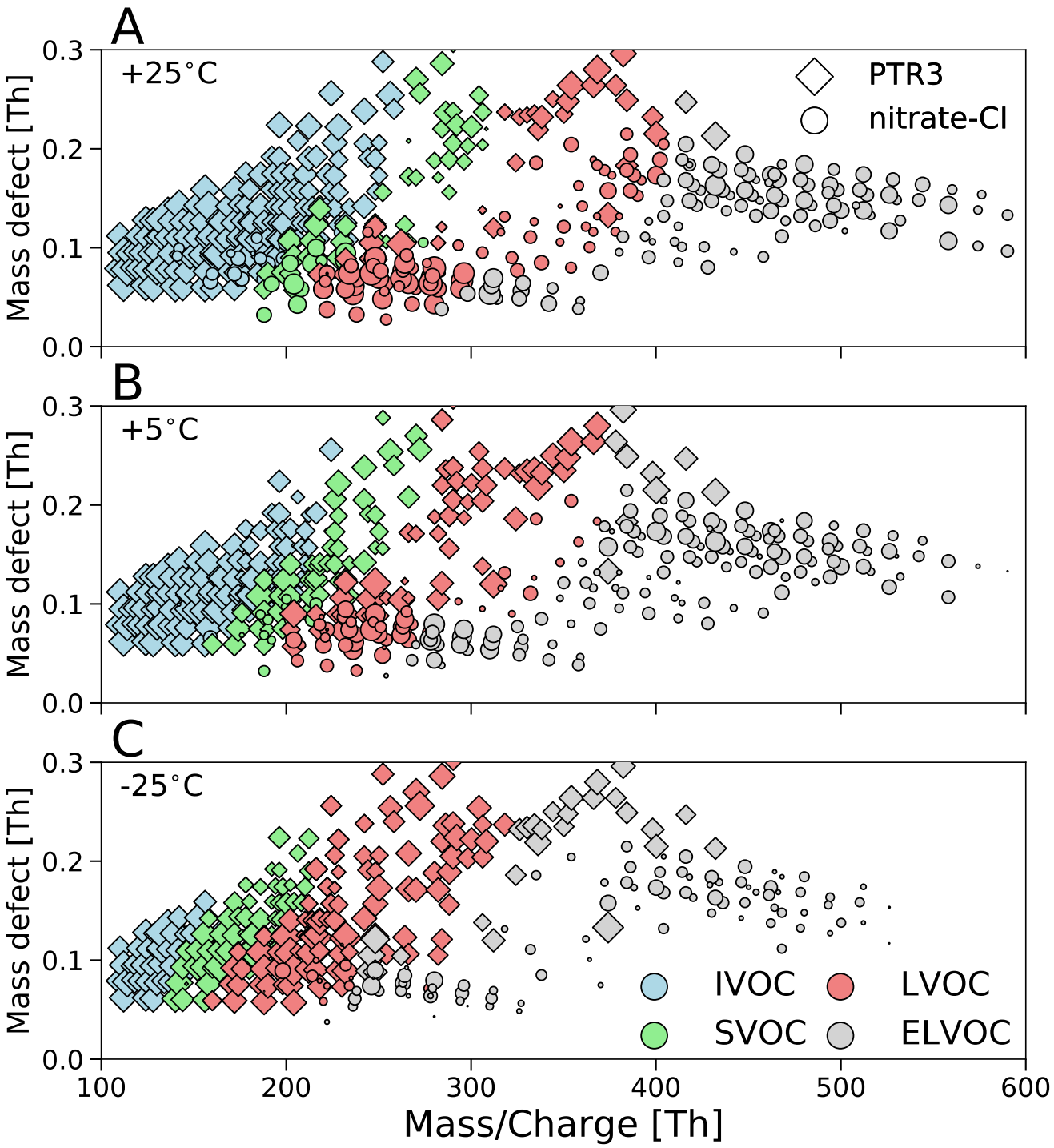

Fig. S4. Mass defect of all measured neutral oxidized organic compounds versus the nominal mass to charge ratio of three representative experiments, at +25°C (A), at +5°C (B) and at -25°C (C), all with a similar α-pinene ozonolysis reaction rate. Diamonds represent molecular ions measured by the PTR3 and circles compounds measured by the nitrate-CI, both taking the different reagent ions into account. The size of the symbols is proportional to the logarithm of the measured concentration and the color is related to the volatility class as defined in Fig. S6.

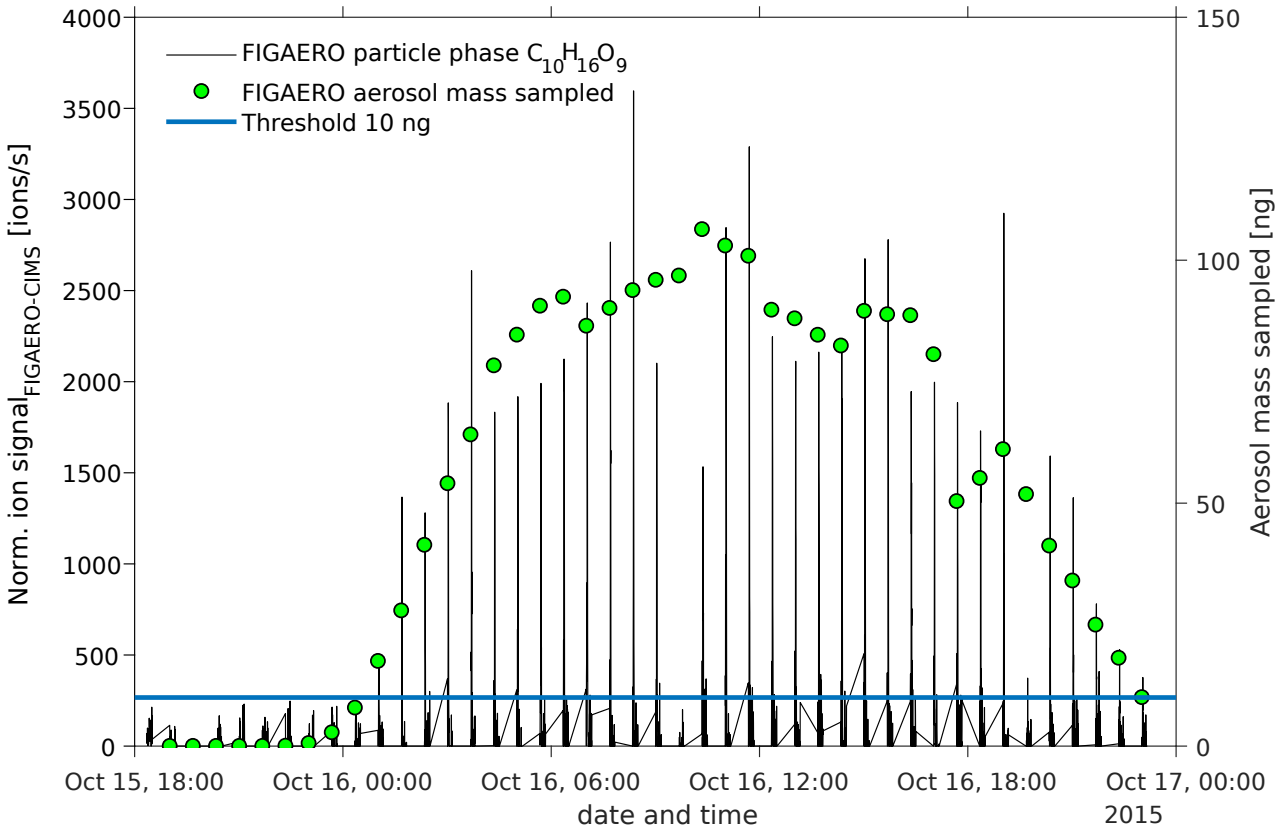

Fig. S5. Time series of $C_{10}H_{16}O_9$ from FIGAERO particle phase measurements showing consecutive thermal desorptions. The blue line indicates the threshold value above which thermograms were normalized on the sampled aerosol mass and used for further analysis.

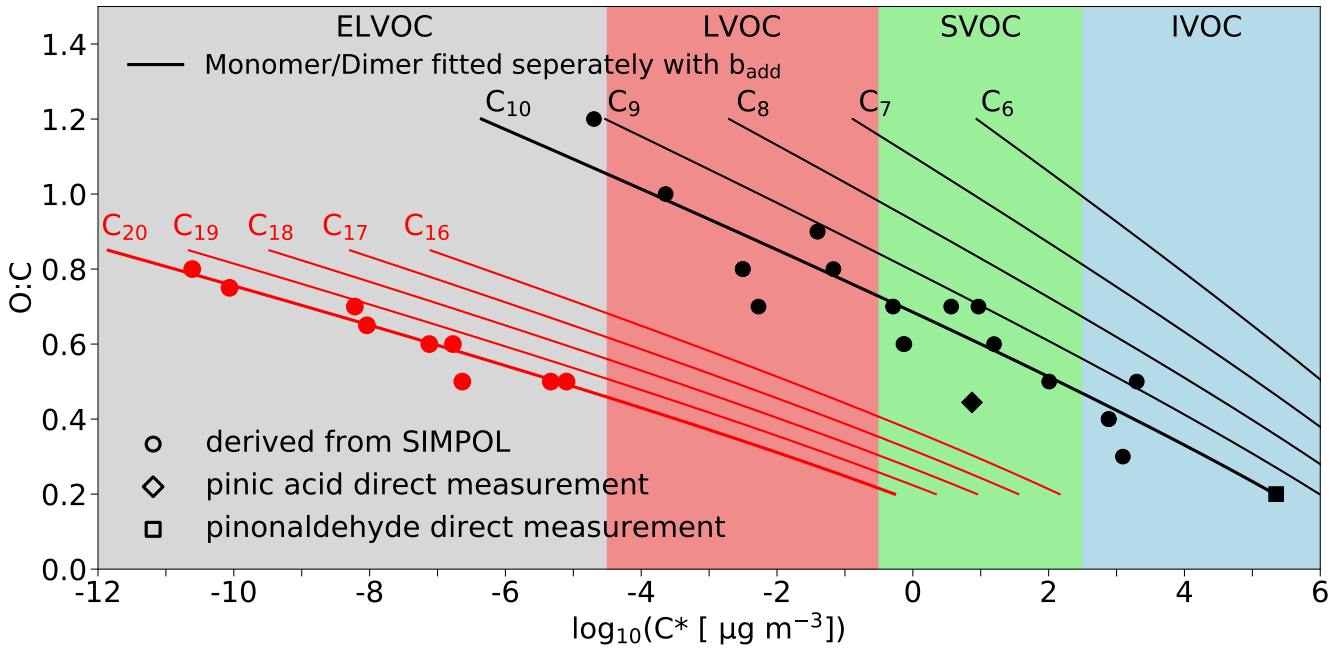

Fig. S6. Volatility model used in this study. For a representative set of proposed products from α-pinene ozonolysis the known structure is used to calculate the volatility by the group-contribution method SIMPOL or are directly measured by (25, 26). Results are fitted with the proposed relationship from (17) including a free parameter for the oxygen dependence.

Table S1. Resulting parameters from least-square regression for the growth rate parametrization of Fig. 2 (A) and (B) by the simple exponential relation $GR = m(T, d_p) \cdot [\mathrm{k}(T) \cdot \mathrm{ap} \cdot \mathrm{O_3}]^q$.

Size-Range	m(+25°C)	m(+5°C)	m(-25°C)	q
1.8-3.2 nm	$1.12{\cdot}10^{-7}$	$2.09{\cdot}10^{-7}$	$2.67{\cdot}10^{-7}$	1.21
3.2-8.0 nm	$2.66{\cdot}10^{-7}$	$3.12{\cdot}10^{-7}$	$3.57{\cdot}10^{-7}$	1.21

References

1. Stolzenburg D, Steiner G, Winkler PM (2017) A DMA-train for precision measurement of sub-10 nm aerosol dynamics. *Atmos. Meas. Tech.* 10(4):1639–1651.
2. Vanhanen J, et al. (2011) Particle size magnifier for nano-cn detection. *Aerosol Sci. Tech.* 45(4):533–542.
3. Tröstl J, et al. (2015) Fast and precise measurement in the sub-20 nm size range using a scanning mobility particle sizer. *J. Aerosol Sci.* 87:75–87.
4. Manninen HE, et al. (2009) Long-term field measurements of charged and neutral clusters using neutral cluster and air ion spectrometer (nais). *Boreal Environ. Res* 14:591–605.
5. Tröstl J, et al. (2016) The role of low-volatility organic compounds in initial particle growth in the atmosphere. *Nature* 533:527–531.
6. Pichelstorfer L, et al. (2018) Resolving nanoparticle growth mechanisms from size- and time-dependent growth rate analysis. *Atmos. Chem. Phys.* 18(2):1307–1323.
7. Lehtipalo K, et al. (2014) Methods for determining particle size distribution and growth rates between 1 and 3 nm using the particle size magnifier. *Boreal Environ. Res.* 19(suppl. B):215–236.
8. Kürten A, Rondo L, Ehrhart S, Curtius J (2011) Performance of a corona ion source for measurement of sulfuric acid by chemical ionization mass spectrometry. *Atmos. Meas. Tech.* 4(3):437–443.
9. Ehn M, et al. (2014) A large source of low-volatility secondary organic aerosol. *Nature* 506:476–479.
10. Kürten A, Rondo L, Ehrhart S, Curtius J (2012) Calibration of a chemical ionization mass spectrometer for the measurement of gaseous sulfuric acid. *J. Phys. Chem. A* 116(24):6375–6386. PMID: 22364556.
11. Heinritzi M, et al. (2016) Characterization of the mass-dependent transmission efficiency of a cims. *Atmos. Meas. Tech.* 9(4):1449–1460.
12. Gormley PG, Kennedy M (1948) Diffusion from a stream flowing through a cylindrical tube. *P. Roy. Irish Acad. A* 52:163–169.
13. Breitenlechner M, et al. (2017) PTR3: An instrument for studying the lifecycle of reactive organic carbon in the atmosphere. *Anal. Chem.* 89(11):5824–5831. PMID: 28436218.
14. Hyttinen N, Rissanen MP, Kurtén T (2017) Computational comparison of acetate and nitrate chemical ionization of highly oxidized cyclohexene ozonolysis intermediates and products. *J. Phys. Chem. A* 121(10):2172–2179. PMID: 28234483.
15. Frege C, et al. (2018) Influence of temperature on the molecular composition of ions and charged clusters during pure biogenic nucleation. *Atmos. Chem. Phys.* 18(1):65–79.
16. Praske E, et al. (2018) Atmospheric autoxidation is increasingly important in urban and suburban north america. *P. Nat. Acad. Sci. USA* 115(1):64–69.
17. Donahue NM, Epstein SA, Pandis SN, Robinson AL (2011) A two-dimensional volatility basis set: 1. organic-aerosol mixing thermodynamics. *Atmos. Chem. Phys.* 11(7):3303–3318.
18. Lopez-Hilfiker FD, et al. (2014) A novel method for online analysis of gas and particle composition: description and evaluation of a Filter Inlet for Gases and AEROsols (FIGAERO). *Atmos. Meas. Tech.* 7(4):983–1001.
19. Stark H, et al. (2017) Impact of thermal decomposition on thermal desorption instruments: Advantage of thermogram analysis for quantifying volatility distributions of organic species. *Environ. Sci. Technol.* 51(15):8491–8500. PMID: 28644613.
20. Goodman KJ, Brenna JT (1994) Curve fitting for restoration of accuracy for overlapping peaks in gas chromatography/combustion isotope ratio mass spectrometry. *Anal. Chem.* 66(8):1294–1301. PMID: 8210045.
21. Pankow J, Asher W (2008) SIMPOL.1: a simple group contribution method for predicting vapor pressures and enthalpies of vaporization of multifunctional organic compounds. *Atmos. Chem. Phys.* 8:2773–2796.
22. Kurtén T, et al. (2016) Alpha-pinene autoxidation products may not have extremely low saturation vapor pressures despite high O:C ratios. *J. Phys. Chem. A* 120(16):2569–2582. PMID: 27049168.
23. Epstein SA, Riipinen I, Donahue NM (2010) A semiempirical correlation between enthalpy of vaporization and saturation concentration for organic aerosol. *Environ. Sci. Technol.* 44(2):743–748. PMID: 20025284.
24. Fuchs N, Sutugin A (1965) Coagulation rate of highly dispersed aerosols. *J. Colloid Sci.* 20(6):492 – 500.
25. Hallquist M, Wängberg I, Ljungström E (1997) Atmospheric fate of carbonyl oxidation products originating from alpha-pinene and delta-3-carene: Determination of rate of reaction with OH and NO3 radicals, UV absorption cross sections, and vapor pressures. *Environ. Sci. Technol.* 31(11):3166–3172.
26. Bilde M, Pandis SN (2001) Evaporation rates and vapor pressures of individual aerosol species formed in the atmospheric oxidation of alpha- and beta-pinene. *Environ. Sci. Technol.* 35(16):3344–3349. PMID: 11529575.